2-1-2020

Three-Dimensional Viscoelastic Instabilities in a Four-Roll Mill Geometry at the Stokes Limit

Paloma Gutierrez-Castillo
University of California, Davis

Adam Kagel
University of California, Davis

Becca Thomases
University of California, Davis, bthomases@smith.edu

RESEARCH ARTICLE | FEBRUARY 03 2020

Three-dimensional viscoelastic instabilities in a four-roll mill geometry at the Stokes limit

Paloma Gutierrez-Castillo ; Adam Kagel; Becca Thomases

Physics of Fluids 32, 023102 (2020)
https://doi.org/10.1063/1.5134927

Physics of Fluids ARTICLE scitation.org/journal/phf

Three-dimensional viscoelastic instabilities in a four-roll mill geometry at the Stokes limit

Cite as: Phys. Fluids 32, 023102 (2020); doi: 10.1063/1.5134927
Submitted: 4 November 2019 • Accepted: 9 January 2020 •
Published Online: 3 February 2020

Paloma Gutierrez-Castillo,[a] Adam Kagel,[b] and Becca Thomases[c]

AFFILIATIONS

Department of Mathematics, University of California, Davis, California 95616, USA

[a]Author to whom correspondence should be addressed: pgutierrez@math.ucdavis.edu
[b]ackagel@ucdavis.edu
[c]thomases@math.ucdavis.edu

ABSTRACT

Three-dimensional numerical simulations of viscoelastic fluids in the Stokes limit with a four-roll mill background force (extended to the third dimension) were performed. Both the Oldroyd-B model and FENE-P model of viscoelastic fluids were used. Different temporal behaviors were observed depending on the Weissenberg number (non-dimensional relaxation time), model, and initial conditions. Temporal dynamics evolve on long time scales, and simulations were accelerated by using a Graphics Processing Unit (GPU). Previously, parameter explorations and long-time simulations in 3D were prohibitively expensive. For a small Weissenberg number, all the solutions are constant in the third dimension, displaying strictly two-dimensional temporal evolutions. However, for a sufficiently large Weissenberg number, three-dimensional instabilities were observed, creating complex temporal behaviors. For certain Weissenberg values and models, the instability that first emerges is two-dimensional (in the x, y plane), and then the solution develops an instability in the z-direction, whereas for others the z instability comes first. Using a linear perturbation from a steady two-dimensional background solution, extended to three dimensions as constant in the third dimension, it is demonstrated that there is a linear instability for a sufficiently large Weissenberg number, and possible mechanisms for this instability are discussed.

I. INTRODUCTION

It is well known that viscoelastic fluids can develop instabilities and time-dependent flows even in the creeping flow regime (very low Reynolds number). It is thought that these instabilities can be used to enhance mixing at micro-scales, which is difficult in Newtonian fluids.

Although the mixing properties and dynamics of viscoelastic fluids have been studied experimentally, theoretically, and numerically, a complete picture of the purely elastic instabilities in the low Reynolds number regime has not emerged. Numerical simulations in two spatial dimensions are the most well-studied, and there are far fewer numerical studies in three dimensions. Analysis of instabilities of 3D flows at extensional points are nearly absent in the literature.

Note that even in experiments of fluids that exhibit three-dimensional flows, it is difficult to measure all three dimensions simultaneously. Only some of the newest techniques have been able to analyze the fully three-dimensional flows.[1] See Ref. 2 for a recent review of the state of the art of the three-dimensional viscoelastic instabilities in micro-channels, which is one of the main applications where low Reynolds number instabilities are studied.

Numerical studies have shown the importance of varying the height of the third dimension in different kinds of micro-fluidic channels. In Ref. 3, the authors perform three-dimensional simulations of viscoelastic fluids in a contraction channel. They showed that varying the aspect ratio of the channel has similar effects to varying other parameters, such as fluid properties, which influence the elasticity number. Specifically, they simulate a three-dimensional flow (Re = 0.465) passing through a planar contraction micro-channel. They observe a transition in the vortex mechanism from a salient-corner to a lip vortex mechanism as the aspect ratio is varied from an ideal 2-D flow to a strongly 3-D flow.

One of the most significant applications of micro-scale instabilities in non-Newtonian fluids is the mixing enhancement. Some recent three-dimensional simulations have been instrumental in understanding this effect. For example, the first three-dimensional DNS (Direct Numerical Simulation) study of a viscoelastic flow in a curvilinear channel driven by a constant pressure gradient was performed by Ref. 4 obtaining a good agreement with the experimental data (even though they introduced an artificial dissipation effect). Then, they explored the relationship between the purely elastic instability and the effect of obtaining a mixing enhancement. They have seen how above a critical Weissenberg number (Wi, non-dimensional relaxation time) there exists a strong unstable secondary flow in the cross-section perpendicular to the streamwise direction, resulting in a strong mixing enhancement.

Furthermore, evidence of the importance of the third dimension in another application of viscoelastic flows can be found in Ref. 5, where simulations for polymer extrudate, which swell out of slit dies from low to high aspect ratios, were performed. It was shown that increasing the aspect ratio of the die geometry (width/height ratio variation from 1 to 20) contributes to a significant change in the 3D extrudate deformation (relative changes of 10% in several directions; absolute changes up to 30%) and delays the equilibrium axial position (up to a factor 10).

Experimentally, even though the devices are three-dimensional, measuring the whole three-dimensional field is not possible, and only some planes are generally accessible. There exists a very recent study,[1] in which they used a three-dimensional holographic particle velocimetry to study the three-dimensional flow field in the case of flow past a cylinder allowing to reproduce the three-dimensional velocity fields. Besides, being a benchmark for non-Newtonian fluids, the flow around a cylinder mechanism is not well understood. With the three-dimensional velocity fields, they have seen more complex flow transitions that could previously be inferred from two-dimensional measurements. They reported three main discoveries of the elastic instability upstream of a single cylinder, including the demonstration of the propagation of an elastic wave, which provides a mechanism by which perturbations can travel upstream. The elastic wave is found to increase in speed and penetrate farther upstream with Wi, indicating an absolute instability emanating from the cylinder. Note that the discoveries of the mechanisms of instabilities in one geometry, such as planar contractions, can help the understanding of the study of the instabilities of the flow around the cylinder and vice versa. However, there are differences between the flow around a cylinder and contraction type flows since the cylinder separates the flow into two separate streams.

It has been known for a while that there is an influence of the third dimension on instabilities in flows around cylinders. A recent experimental study focuses on the case of flow around the high-aspect-ratio, low-blockage-ratio microfluidic cylinders.[6] They studied the configurations of one and two cylinders and how the influence on each other depends on Wi. Knowing how the instabilities depend on the number of cylinders is especially relevant since a large array of cylinders are often used as a model for porous media. Experimentally, it was shown[7] that a long micro-channel with an array of obstacles shows instabilities in the case of non-Newtonian fluids. More recently, an array of staggered cylinders, similar to a model for porous media, were studied experimentally, see for example Ref. 8. Numerically, when increasing the number of cylinders in the array, the computational cost increases significantly, and thus, most of the numerical studies with a multitude of cylinders are restricted to two dimensions.

Another geometry where there exist pure-elastic instabilities is the three-dimensional cross-slot geometry (and its variants such as the "T" geometry). Low Reynolds number instabilities at extensional points have been observed both experimentally and numerically,[9–11] but the role of the third dimension in these instabilities is not well understood. In Ref. 12, the authors numerically study the three-dimensional flow behavior of $\mathrm{Re} \leq 0.01$. Later, the same group studied experimentally the difference in having two different aspect ratios in the cross-slot geometry.[13]

We have seen that there is significant evidence showing the importance of the third dimension in the viscoelastic creeping flow instabilities. Similar to the cross-slot geometry, i.e., showing pure elastic instabilities at extensional points in two dimensions, is the four-roll mill geometry. This geometry has been shown to present instabilities but also mixing enhancement[14–16] and is a somewhat simple geometry to do some analysis on the flow dynamics.[17,18] In this configuration, four-rollers create an extensional flow at the center of the domain, which will drive elastic instabilities. Here, we extend this geometry to a third dimension to understand the effect of the third dimension on instabilities in the flow. In this case, the domain is still periodic, but now in three dimensions, and the background force is formed by cylinders instead of circles. An examination of this extended geometry was previously discouraged by long-computation times, but our spectral model allows for significant computational speed ups via Graphics Processing Unit (GPU) acceleration of Fast Fourier Transforms (FFTs), described in the Appendix. We focus our study on the creation of an instability in the direction parallel to the cylinders, which is novel with respect to the two-dimensional cases previously studied.

II. FLUID MODELS AND NUMERICAL DETAILS

A. Stokes–Oldroyd-B model

For some of our simulations, we use the Oldroyd-B model of a viscoelastic fluid at zero Reynolds number, with explicit polymer stress diffusion, given in the dimensionless form by

$$\Delta \mathbf{u} - \nabla p + \beta \nabla \cdot \mathbf{S} = \mathbf{f}, \tag{1}$$

$$\nabla \cdot \mathbf{u} = 0, \tag{2}$$

$$\partial_t \mathbf{S} + \mathbf{u} \cdot \nabla \mathbf{S} - \left(\nabla \mathbf{u} \mathbf{S} + \mathbf{S} \nabla \mathbf{u}^T \right) + \mathrm{Wi}^{-1} (\mathbf{I} - \mathbf{S}) = \nu_p \Delta \mathbf{S}, \tag{3}$$

where $\mathbf{u}$ is the fluid velocity, p the fluid pressure, and $\mathbf{S}$ the (symmetric) conformation tensor, a macroscopic average of the polymer orientation and stretching that is related to the polymer stress tensor by $\boldsymbol{\tau}_p = \beta(\mathbf{S} - \mathbf{I})$. The parameters, β, the non-dimensional polymer stiffness, and Wi, the Weissenberg number, or non-dimensional relaxation time, are defined by

$$\beta = \frac{GL}{\mu U}, \quad \mathrm{Wi} = \frac{\lambda U}{L}, \tag{4}$$

where μ is the solvent viscosity, λ the fluid relaxation time, G the polymer elastic modulus, $L = 2\pi$ the system size, and U the characteristic velocity scale. Note that the Oldroyd-B model has $\nu_p = 0$ in Eq. (3). The polymer stress diffusion term, $\nu_p \Delta \mathbf{S}$, where $\nu_p = 0.001$, is included in the right-hand side of Eq. (3) as numerical regularization. We will make some comments on the applicability of these results to the case without diffusion and varying resolution in the end of Sec. V B.

The background force is given by

$$\mathbf{f} = \begin{pmatrix} 2\sin x\cos y \\ -2\cos x\sin y \\ 0 \end{pmatrix}, \tag{5}$$

which in a Newtonian Stokes flow ($\beta = 0$) corresponds to a four-roll velocity field $\mathbf{u} = -\frac{1}{2}\mathbf{f}$. The Stokes solution sets the characteristic (inverse) time scale $U/L = 1$. The quantity $\beta \cdot \mathrm{Wi}$ is the ratio of the polymer viscosity to solvent viscosity, so that given a particular working fluid the ratio is fixed independent of the experimental conditions. In our simulations $\beta \cdot \mathrm{Wi} = 0.5$ is fixed. This value is consistent with the fluids used in the experiments of dilute polymer solutions with highly viscous solvents, Boger fluids (see, for example, Ref. 9).

B. FENE-P model

To test the robustness of the instabilities, we found in the Oldroyd-B model, we also use the FENE-P model,[19] and in this case, the advection is performed with the square root method. For the square-root method,[20] the model is reformulated in terms of the (unique) positive symmetric square root $\mathbf{b}(x, t)$ of the conformation tensor $\mathbf{S}(x, t)$, and the evolution of $\mathbf{S}$ given by Eq. (3) is replaced with

$$\left(\frac{\partial}{\partial t} + \mathbf{u}\cdot\nabla\right)\mathbf{b} = \mathbf{b}\nabla\mathbf{u} + \mathbf{a}\mathbf{b} + \frac{1}{2\mathrm{Wi}}\left(\left(b^T\right)^{-1} + \frac{\mathbf{b}}{1 - \|\mathbf{b}\|^2/\ell^2}\right) + \nu_f \Delta\mathbf{b}. \tag{6}$$

The time evolution produces the unique positive symmetric square root of $\mathbf{S}$, when $\mathbf{a}(x, t)$ is any antisymmetric matrix and $\mathbf{b}^T(x, 0)\mathbf{b}(x, 0) = \mathbf{S}(x, 0)$. The key observation is that by choosing $\mathbf{a}(x, t)$ properly, it is possible to tune the evolution [Eq. (6)] (and similarly in other models with an upper convective derivative) to preserve the symmetry of $\mathbf{b}$. Specifically, by choosing a symmetric initial data $\mathbf{b}^T(x, 0) = \mathbf{b}(x, 0)$, the subsequent evolution will preserve the symmetry. We fix the length-scale cut off to be $\ell^2 = 400$. We have also added diffusion to the model, $\nu_f \approx 0.024$. The size of this diffusion coefficient is comparable to the size of the square root of the diffusion coefficient in the Oldroyd-B model.

C. Numerical details

The system Eqs. (1)–(3) [or Eq. (6) for the FENE-P simulations] are solved in a 3D spatially periodic domain, $[0, 2\pi)^3$. Figure 1 shows a schematic of the domain with a background force.

We use a pseudo-spectral method and alternate solving of the Stokes equations for a given polymer stress tensor and time-stepping the advection equation for the conformation tensor in Fourier space using a second order Adams–Bashforth–Crank–Nicholson method. This is the same numerical setup used in Refs. 15 and 16, where 2D solutions were studied and the instabilities in the four-roll mill problem were first observed and more recently in Ref. 21, where the 2D instabilities were described using proper orthogonal decomposition (POD) for both the Oldroyd-B and FENE-P models. We have used the $N^3 = 128^3$ grid points, which give uniform grid spacing $\Delta x = 2\pi/N \approx 0.05$ and time step $\Delta t = 0.005$. To demonstrate the accuracy of the spatial resolution, a refinement study is shown in Fig. 2. This figure shows the relative error in the L^2 norm of the velocity and the L^2 norm of the conformation tensor, relative to the $N = 192$ solution of a typical case of Wi = 12. We see that the error decays with increasing refinement and the error is on the 10^{-5} for the two finest reported grids. Note also that the time step was chosen sufficiently small to obtain stability in the method but the dynamics of the problem are very slow with periods on the order of $T = 100$ or longer. Therefore, there are over 20 000 time steps in a period.

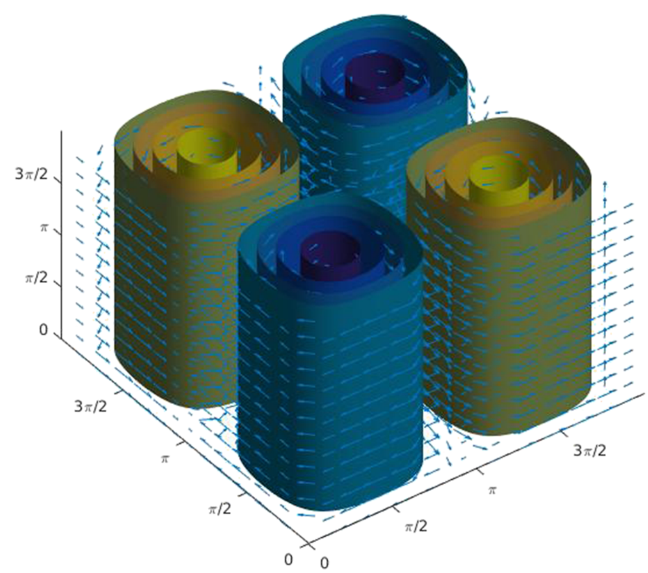

FIG. 1. Schematic of the setup showing the background force. Periodic boundary conditions are assumed in x, y, z.

To compute the solutions for Oldroyd-B, we start from a random perturbation of the low Fourier modes from isotropic initial polymer stress $\mathbf{S} = \mathbf{I}$. Specifically, we randomly perturb 25 of the modes with frequencies smaller than 8 in all the directions. Therefore, the polymer stress with the perturbation $\tilde{\mathbf{S}}$ can be written as $\mathbf{S} = \mathbf{I} + \tilde{\mathbf{S}}$, where the diagonal terms of the perturbation are computed by

$$\tilde{S}_{ii} = \sum_{k=1}^{25} C_k \sin(\omega_{k_x} x)\sin(\omega_{k_y} y)\sin(\omega_{k_z} z),$$

where x, y, and z are spatial coordinates,ω_{k_x}, ω_{k_y}, and ω_{k_z} are randomly selected from 1 to 8, and C_k is randomly selected in Fourier space to be $0 < C_k < 10^3$, equivalent to a small perturbation in the physical space. Similarly, the off diagonal terms are defined in the same way but with a different constant $0 < \overline{C}_k < 10^2$. That is,

$$\tilde{S}_{ij} = \sum_{k=1}^{25} \overline{C}_k \sin(\omega_{k_x} x)\sin(\omega_{k_y} y)\sin(\omega_{k_z} z).$$

Adding all these perturbations lead to a perturbation of the order 0.01 of the identity in the physical space.

For FENE-P, we perform these simulations with initial data for the conformation tensor taken from the Oldroyd-B solutions

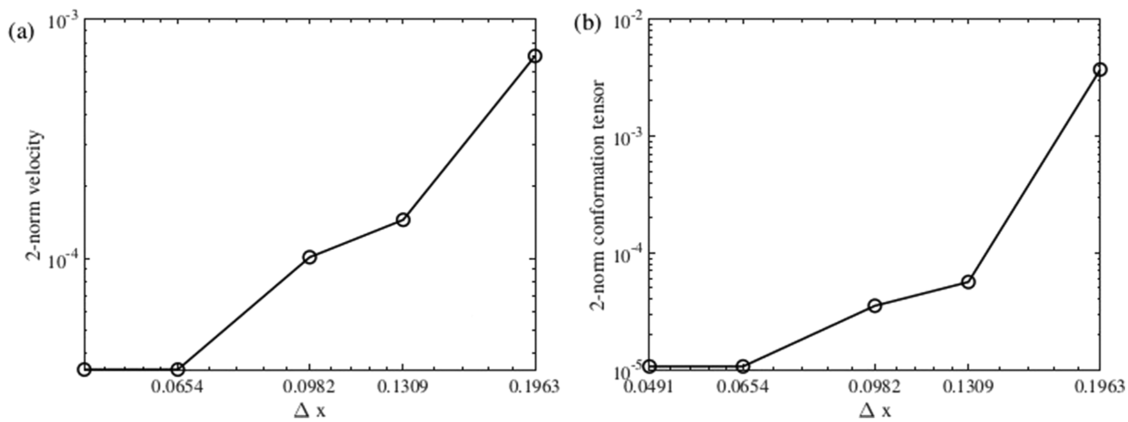

FIG. 2. Grid refinement study. Errors computed by comparing with the finest resolution N = 192, (a) L^2 norm of the velocity, (b) L^2 norm of the conformation tensor.

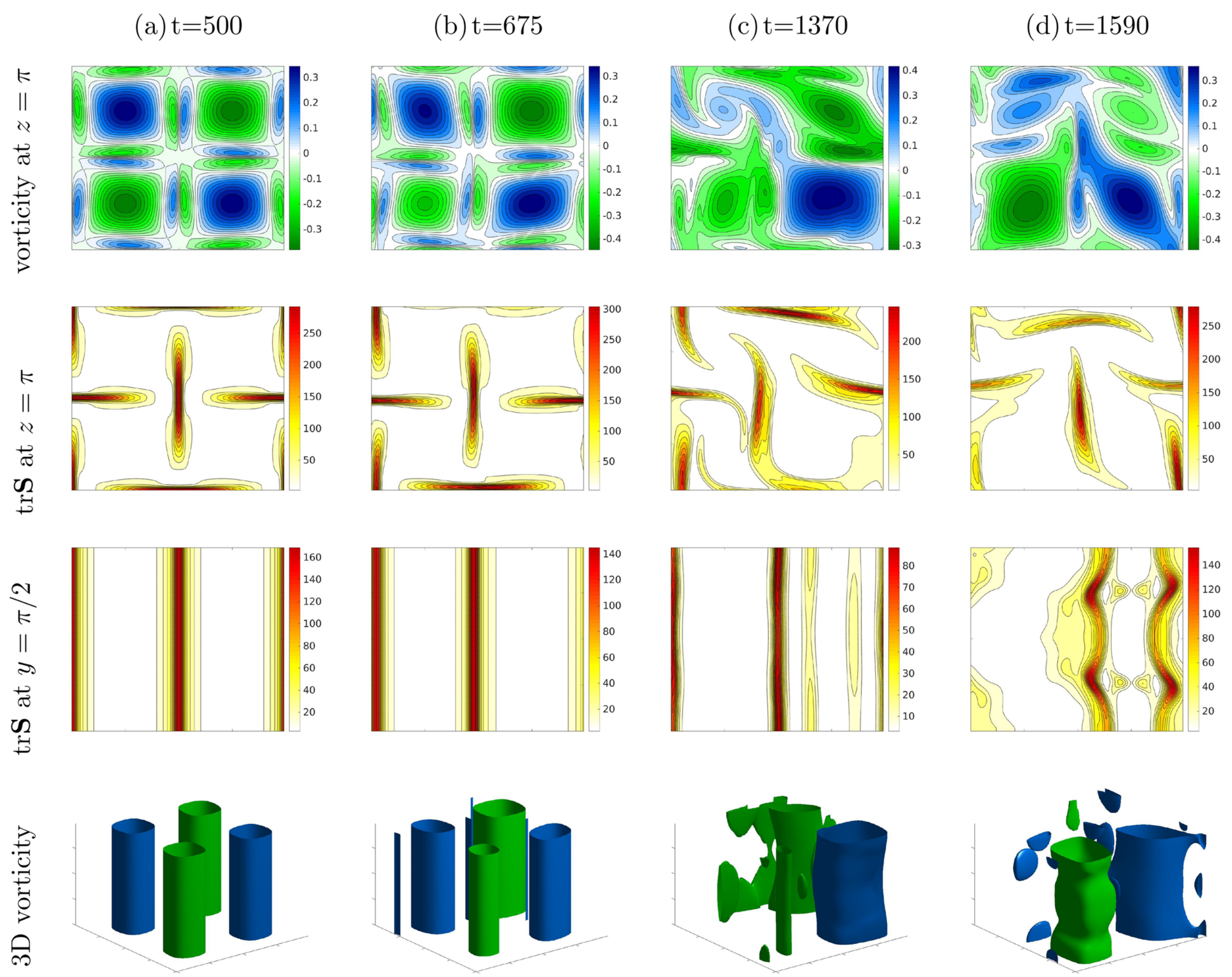

FIG. 3. Solution for Wi = 8 at (a) t = 500, (b) t = 675, (c) t = 1370, and (d) t = 1590. First row: Contours of azimuthal vorticity at $z = \pi$. Second row: contours of tr**S** at $z = \pi$. Third row: contours of tr**S** at $y = \pi/2$. Fourth row: isosurfaces of azimuthal vorticity for the values of ±0.20. Multimedia views (a): https://doi.org/10.1063/1.5134927.1; (b): https://doi.org/10.1063/1.5134927.2

TABLE I. Categorization of flow states found with simulations of the Oldroyd-B model in 3D. Flow is forced with a 2D four-roll mill that is constant in *z*.

Wi range	# Flow transitions	*x*, *y* dynamics	*z*-dynamics
Wi ≤ 5	0	Steady 2 symmetries	Steady and constant
Wi = 6	1	Steady 1 symmetry	Steady and constant
Wi = 7	2	Quasi-steady 1 symmetry then unstable	Steady and constant
8 ≤ Wi < 10	2	Unstable in 2D	Temporal *z*-dependence after 2D instability
10 ≤ Wi ≤ 12	2	Unstable in 2D	Temporal *z*-dependence before 2D instability

both with and without instability in the *z* direction (with the intermediate step of computing the symmetric square root to the stress tensor).

The dynamics in this problem occur on very long time scales, and to capture the slow dynamics, we run our simulations up to at least $t = 4000$ and in some cases longer. The wide parameter searches and long time evolutions made this exploration prohibitively expensive in the past. Here, we use the GPU acceleration of Fast Fourier Transforms (FFTs), which in our spectral model allows for significant computational speed ups. The details are described in the Appendix.

III. RESULTS FOR OLDROYD-B

In this section, we report on the results obtained using the Oldroyd-B model when varying Wi ≤ 12. In particular, we want to analyze in detail the cases that develop instability in the *z*-direction. This instability is new with respect to the 2D cases analyzed previously in the literature.[15,16,21]

A. Cases with no *z*-instability (Wi < 8)

For Wi < 8, there is no instability in the third dimension. Note that since the same 4-roll mill geometry is prescribed in the *x*, *y* plane for all *z*, any flow dependence in the *z*-direction is what we refer to as the fully three dimensional solution. The results for Wi < 8 remain constant in *z*, which we refer to as purely 2D. These results are similar to the 2D results presented in previous papers.[15,16,21] As in the 2D simulations, here it was found that for Wi ≤ 5, the flows remain in a steady symmetric state formed by 4-roll cylinders, the arrangement of the flow is similar to that shown in Fig. 3(a) (Multimedia view). As in the 2D simulations for Wi = 6, the flow becomes unstable in the *x*, *y* plane and, in the long term, produces a flow that is steady but asymmetric and remains constant in *z*. For 7 ≤ Wi < 8, the flow is still two-dimensional, but it has 2D instabilities that persist in time and are temporally quasi-periodic with a dominant vortex changing its position in the *x*, *y* plane. A summary of the different flow states observed is given in Table I.

B. Three-dimensional instabilities

1. 2D instability followed by a 3D instability (8 ≤ Wi < 10)

The first three-dimensional instability was observed for Wi = 8. At early times, the flow remains in a quasi-steady state with a symmetric 4-roll pattern. See Fig. 3(a) (Multimedia view) for a solution at $t = 500$ before the onset of any time-dependent behavior. The first row shows contours of the azimuthal vorticity at $z = \pi$, where the 4-roll symmetric structure is clear. The second row shows tr**S** at the same time, and the typical regions of the concentrated stress, large tr**S**, can be observed. Note here that using horizontal cuts at the center of the domain, it is useful to compare with the 2D simulations. However, this is not sufficient to describe the three-dimensional solution. Therefore, vertical cuts and 3D isosurfaces are presented here to better describe the solution structure. Specifically, the third row of Fig. 3 shows tr**S** in a vertical plane, and the last row shows isosurfaces of vorticity. With the vertical cuts and the isosurfaces, at $t = 500$, we see that there is no three-dimensional behavior in the flow (i.e., the solution is constant in *z*).

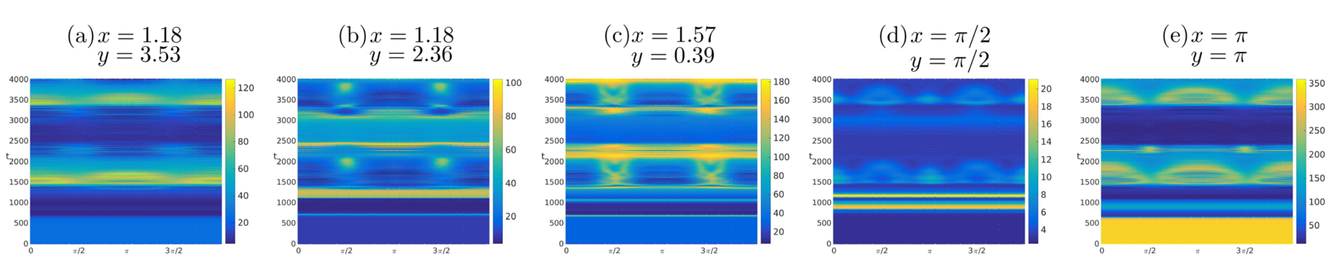

FIG. 4. Time evolution of the *z*-axis for tr**S** at different *x*, *y* locations for Wi = 8: (a) $x = 1.18$ $y = 3.53$, (b) $x = 1.18$ $y = 2.36$, (c) $x = 1.57$ $y = 0.39$, (d) $x = \pi/2$ $y = \pi/2$, and (e) $x = \pi$ $y = \pi$.

At later times, the flow undergoes a 2D instability, where it loses the 4-roll symmetric pattern at around t = 550 and one of the vortices becomes dominant. See, for example, Fig. 3(b) (Multimedia view) for a solution at t = 675, where the top-right vortex is dominant. The dominant vortex starts rotating to different positions (similar to the instability found in the 2D simulations of Wi = 7 described in Ref. 21). Then, around t = 1200, the flow becomes three-dimensional perturbing the cylindrical isosurfaces. See, for example,

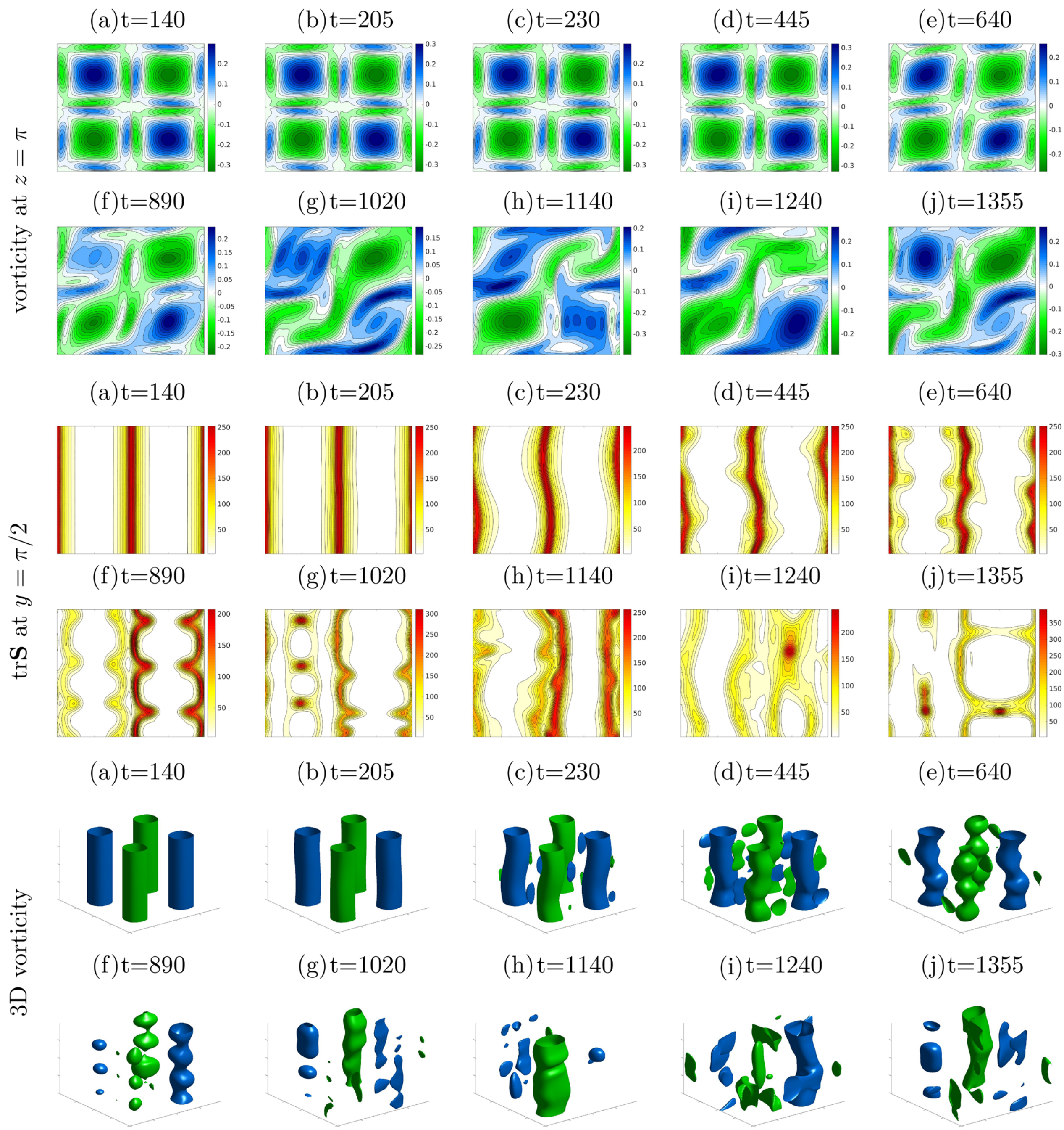

FIG. 5. Solution for Wi = 12 at (a) t = 140, (b) t = 205, (c) t = 230, (d) t = 445, (e) t = 640, (f) t = 890, (g) t = 1020, (h) t = 1140, (i) t = 1240, and (j) t = 1355. First and second row: Contours of azimuthal vorticity at $z = \pi$. Third and fourth row: vertical contours of tr**S** at $y = \pi/2$. Fifth and sixth row: 3D isosurfaces of azimuthal vorticity for the values ±0.20. Multimedia views (a): https://doi.org/10.1063/1.5134927.3; (b): https://doi.org/10.1063/1.5134927.4

Fig. 3(c) for a solution at t = 1370. In this case, this 3D motion is occurring simultaneously with the rotation of the dominant vortex making the flow pattern difficult to describe. See Fig. 3(d) for a solution at t = 1590, where the dominant vortex is now in a different quadrant and the vortex tube pinching is at different heights from that shown in Fig. 3(c). For details of the temporal dependence, see the movies (Multimedia view).

An interesting way to visualize the evolution of the z instability is to look at the time evolution of tr**S** along the z-axis for a fixed x, y location. While we have reviewed the evolution of the z-axis in the whole x, y domain, we display only a few of these time evolutions (see Fig. 4). We choose some singular points such as the one at the center of a roll $(x, y) = (\pi/2, \pi/2)$, as well as at the extensional point in the center of the domain $(x, y) = (\pi, \pi)$ along with three more generic points at $(x, y) = (1.18, 3.53)$, $(x, y) = (1.18, 2.36)$, and $(x, y) = (1.57, 0.39)$, respectively. The rest of the z, t slices show a consistent pattern with the ones presented here. It is evident that for early times ($t < 550$) tr**S** is constant in time for each x, y position since at that stage the behavior of the flow is quasi-steady. Later for $550 \le t \le 1200$, the value of the tr**S** change with time but it is constant along the z axis, corresponding with times where we have a two-dimensional instability with a rotating dominant vortex. For the latest times ($t > 1200$), it is clear how the flow is evolving with time, and it also presents a non-uniform pattern along the z direction. In that range of times, both instabilities are acting simultaneously. Note here that for all the studied cases, the instability in the z-direction was always found to be a low frequency instability, i.e., the created pattern in that area is periodic in the z-direction with period $2\pi/n$, where n is the frequency number.

2. 3D instability first (Wi ≥ 10)

For cases with Wi ≥ 10, the flow develops first the z instability before it becomes unstable in the x, y plane. Contour plots of the vorticity, tr**S**, vertical slices as well as isosurfaces for Wi = 12 are shown in Fig. 5. Initially, the flow remains a quasi-steady symmetric flow [Fig. 5(a) (Multimedia view)]. Then, around t = 205, a three-dimensional flow instability appears. This instability is most clear in the representations of 3D isosurfaces of vorticity, where the original cylinder appears to be bending [Fig. 5(b) (Multimedia view)]. This bending is even more evident later, e.g., in Fig. 5(c). When looking at the details of the solutions, we can appreciate both the bending and pinching effects of the cylinders [see Fig. 5(d)], t = 445. It is important to remark here that at these times, still, the four vortices have similar magnitude as is most clear in the 2D representations at the central z plane. For further times, around t = 775, one of the vortex starts being weaker and another one stronger, as was typically found in the 2-dimensional time evolutions. This effect leads to complex evolutions for further times, where both the z and the x, y temporal evolutions are simultaneously creating a flow where there is bending in the vortex tubes, pinching, and some vortex dominates the others. See sequence of Figs. 5(f)–5(i).

The vertical cuts for Fig. 5 are also very useful to see how the z-dependence evolves with time. For some cases, for example, Fig. 5(f), an instability with frequency 3 is appreciable as cells in tr**S**. At this instant, each of the cells (corresponding to strong pinching) has roughly the same size. This instability is also observable in the vortex tube where the isosurface structure has similarly sized "beads" of constant vorticity. Subsequently, these "beads" periodically increase and decrease in size [see Fig. 5(g)]. For further times [Fig. 5(h)], the pinching is not so strong in the dominant vortex creating a pattern that looks more like tubes than cells (see the 3D vorticity plot). Later, the tubes evolve to more asymmetric solutions in the z direction [Fig. 5(i)], and they recover a two-mode cell pattern [Fig. 5(j)]. This process of creating and destroying cells with spatial frequencies 2 or 3 continues in time (our simulations ran to t = 4000), creating complicated flow patterns. See also the movies (Multimedia view).

Figure 6 shows the time evolution of tr**S** as a function of z for fixed x, y with Wi = 12 for different x, y locations. We see the flow becoming unstable in the z direction around t = 205, developing three-dimensional time-dependent behavior. Note that since there is no significant displacement in the x and y directions at early times, there are no large changes in tr**S** values from one time to the next (see the bottom section of Fig. 6 advancing in the vertical direction). At about t = 775, when the dominant vortex starts rotating, the displacement visible in the time evolution of tr**S** shows additional features. We can see variations in tr**S** when comparing values at the same time and with different z, but also when comparing different times and maintaining the same z. Together with Fig. 5, this paints the picture that the regions of large stress are rotating along with the dominant vortex around the four cylinders, but there is also variation along the z-axis of this rotation and the stress concentration. When the dominant vortex is passing through a particular x, y position, the value of tr**S** is larger along the z-axis compared with those times, when a weak vortex is passing that x, y position. This behavior persists in time.

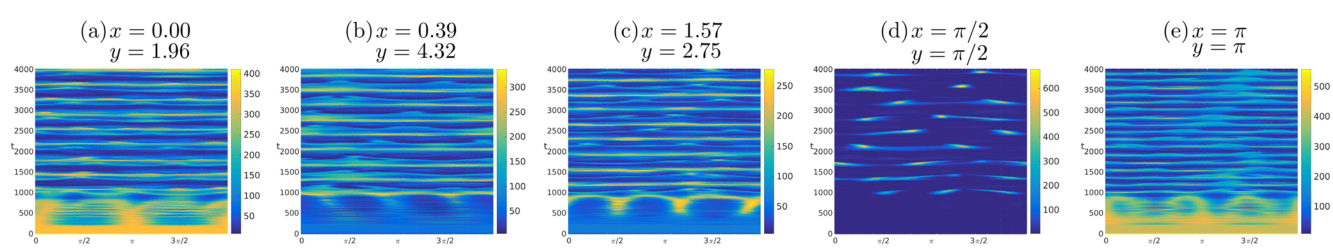

FIG. 6. Time evolution of the z-axis for tr**S** at different x, y locations for Wi = 12: (a) x = 0.00 y = 1.96, (b) x = 0.39 y = 4.32, (c) x = 1.57 y = 2.75, (d) $x = \pi/2$ $y = \pi/2$, and (e) $x = \pi$ $y = \pi$.

IV. FENE-P RESULTS

We found that there is no z-instability for Wi < 12 for the FENE-P model, but we find the z-instability for Wi = 12. In simulations with Wi = 12, the z-instability persists in time, but now we find periodic temporal behavior. Different initial conditions were used, all arriving at different final states that are periodic. In these states, the z-instability is persistent, and there is no sign of the

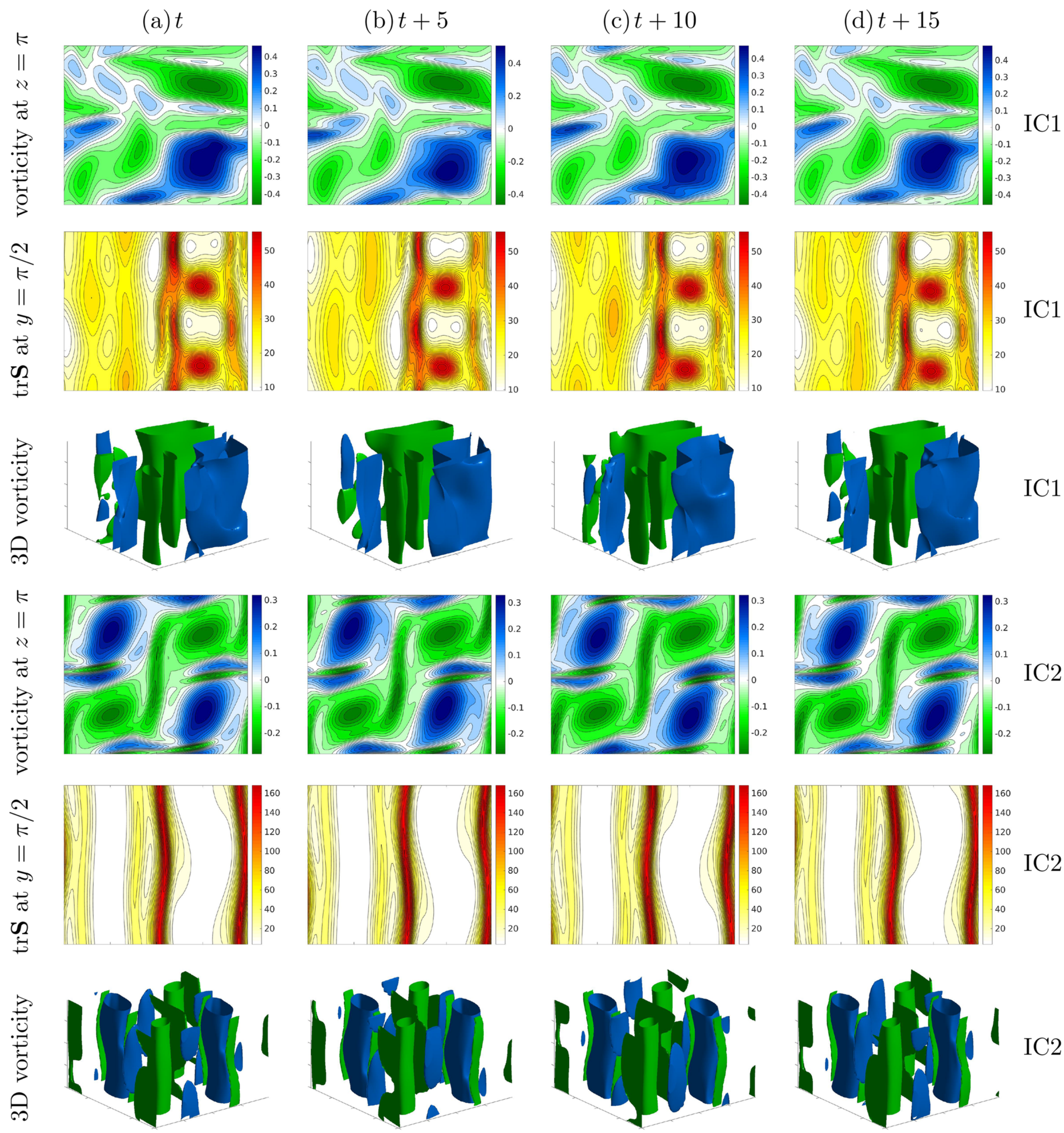

FIG. 7. Time evolution azimuthal vorticity at $z = \pi$, tr**S** at a vertical plane $y = \pi/2$, and 3D isosurfaces of azimuthal vorticity for the values ±0.20 with FENE-P Wi = 12. The first group starting from the initial condition of Oldroyd-B solution for Wi = 8 at t = 4000. The second group starting from the initial condition of Oldroyd-B solution for Wi = 10 at t = 100. (a) t, (b) t + 5, (c) t + 10, and (d) t + 15. Multimedia views: https://doi.org/10.1063/1.5134927.5; https://doi.org/10.1063/1.5134927.6; https://doi.org/10.1063/1.5134927.7; https://doi.org/10.1063/1.5134927.8

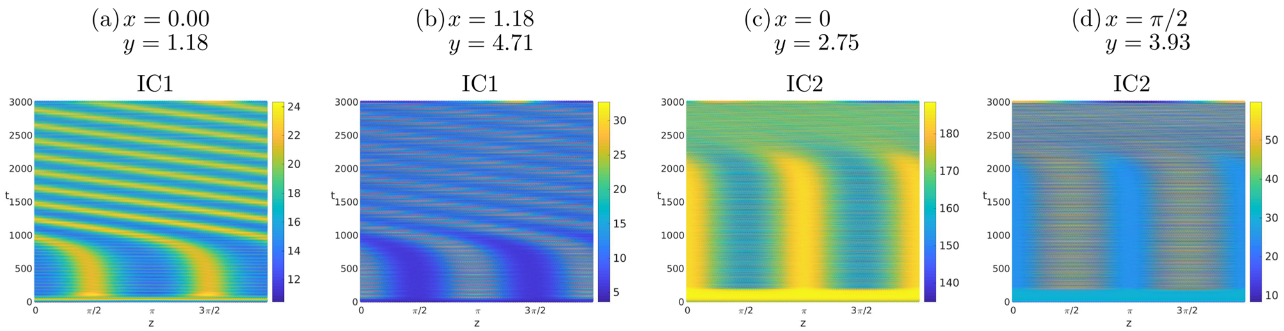

FIG. 8. Time evolution of the *z*-axis for tr**S** at different *x*, *y* locations for Wi = 12, FENE-P. (a) $x = 0.00$ $y = 1.18$ IC1, (b) $x = 1.18$ $y = 4.71$ IC1, (c) $x = 0.00$ $y = 2.75$ IC2, and (d) $x = \pi/2$ $y = 3.93$ IC2.

dominant vortex rotating around the four cylinders as in some of the Oldroyd-B solutions. Figure 7 (Multimedia view) shows snapshots of the fully developed periodic flow for two solutions obtained for Wi = 12 using the FENE-P model. These two different results come from using two different initial conditions. The first initial condition, hereafter IC1, uses an initial conformation tensor taken from solutions to the Oldroyd-B model with Wi = 8 at $t = 4000$; at this point, the 2D flow asymmetry and z-spatio-temporal behavior has already begun. The second initial condition, hereafter IC2, comes from an early solution with Wi = 10 and $t = 200$, where the 2D symmetry break and z-dependence have not yet happened. In Fig. 7 (Multimedia view), the first row of each group shows the vorticity at $z = \pi$, over nearly a period where it is appreciable that there is no rotation of the main vortex for any solution. The following rows display a vertical plane of tr**S** passing through $y = \pi/2$. The z-dependence shows 2 modes in the right-hand side of the IC1 solution. Finally, the 3D representations of the vorticity are shown, where the z-instability and periodicity of the solutions can be seen by the eye. Note here that the solutions are displayed in a time interval of $\Delta t = 5$, which is not necessarily a fraction of the period of the solution; therefore, the first and last figures of each row are not exactly equal. See also the movies (Multimedia view).

Figure 8 shows the time evolution of the z-axis for fixed x, y, Wi = 12, and different initial conditions, demonstrating the periodic temporal behavior. Note that the z positions were picked arbitrarily, and other locations show similar behavior. When comparing the FENE-P temporal behavior shown in Fig. 8 with the Oldroyd-B simulation in Fig. 6, we note that the FENE-P solutions show traveling waves in the z-axis and no evidence of the rotating vortices was seen in Oldroyd-B.

V. CHARACTERIZING THE INSTABILITY IN THE z-DIRECTION

In order to characterize the instability in the z-direction, we focus on an extensional point in the flow. Here, we focus on $(x, y) = (\pi, \pi)$ and examine the behavior of the stress and velocity at the onset of the z-dependence. We will first examine the nonlinear simulations presented in Sec. III B 1 and Sec. III B 2 for Wi = 8, 12, and then, we will consider a linearized problem that is related to the transition we see for Wi = 12.

A. Onset of instability in nonlinear simulations

In Fig. 9(a), we plot the S_{11}, S_{12}, S_{22} components of the stress tensor at the central stagnation point $(x, y) = (\pi, \pi)$ at $z = 0.88$ (an arbitrarily chosen z value) over time for the Wi = 8, Oldroyd-B simulation. At $t \approx 1300$, we note that these components of the stress tensor begin to depend on z. This is correlated with the growth of the $|S_{13}|$, $|S_{23}|$, $|S_{33} - 1|$ components of the stress tensor deviating away from the 2D solution, which has $S_{13} = S_{23} = 0$ and $S_{33} = 1$. We note that all the components of the stress tensor were initially perturbed, but these three components reach zero rapidly and remain zero as long as the flow remains quasi-2D. The onset of the z-instability corresponds with the growth of these stress components. This is seen as well for Wi = 12, shown in Fig. 10. We plot the separate components of S_{11}, S_{12}, S_{22} due to their different scales. In this case, the flow is initially symmetric (in 2D and constant in z) as is seen in Fig. 5(a) (after some transient due to the initial perturbation), and the flow is steady until the S_{13}, S_{23}, S_{33} components become sufficiently large and begin to affect the constant z-flow state. In Fig. 11, we plot the temporal behavior of $\partial_z u$, $\partial_z v$, $\partial_x w$, $\partial_y w$ at $(x, y) = \pi, \pi$ for $z = 0.88$. These are the components of the velocity gradient that are zero when the flow is quasi-2D, and their growth corresponds to the onset of the z-instability. We note that in these simulations, we have sampled the data to plot with $\Delta t = 5$, which is rather coarse and hence after the onset of the z-dependence, the time series is not well resolved in the figure.

B. Linear perturbations

We have observed that an instability develops in the z-direction for a range of sufficiently large Wi, and we noted that the onset of z-dependence occurs both when the flow in x, y has already transitioned to a quasi-periodic asymmetric state (the example above was for Wi = 8) and when the x, y flow is steady (Wi = 12). The simpler case to analyze is when the x, y flow is steady. Here, we examine a numerical linearized flow where the background state is symmetric in x, y and is steady. To obtain the 3D background solution, we first evolve the Stokes–Oldroyd-B system [i.e., Eqs. (1)–(3)] in two space dimensions to a symmetric steady state with a four-roll mill background force. The arrangement of the flow is similar to that shown in Fig. 3 at $t = 500$ (in 2D). We extend the 2D solutions to 3D by making them constant in z [renaming $\overline{S}_{ij}(x, y)$ to $\overline{S}^0_{ij}(x, y, z)$,

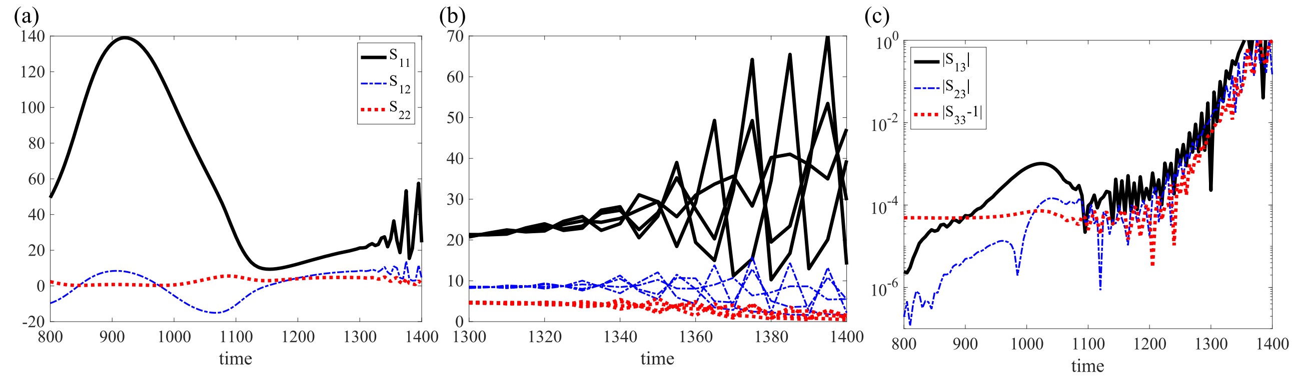

FIG. 9. Data from Oldroyd-B simulation described in Sec. III B 1 for Wi = 8. (a) Temporal behavior of S_{11}, S_{12}, S_{22} components of the conformation tensor at $(x, y) = (\pi, \pi)$ for $z = 0.88$. (b) Temporal zoom of the data from (a) but plotted at 4 different z values between 0.88 and 3.14. (d) Temporal behavior of $|S_{13}|$, $|S_{23}|$, $|S_{33} - 1|$ components of the conformation tensor at $(x, y) = (\pi, \pi)$ for $z = 0.88$; note the log scale on the y-axis.

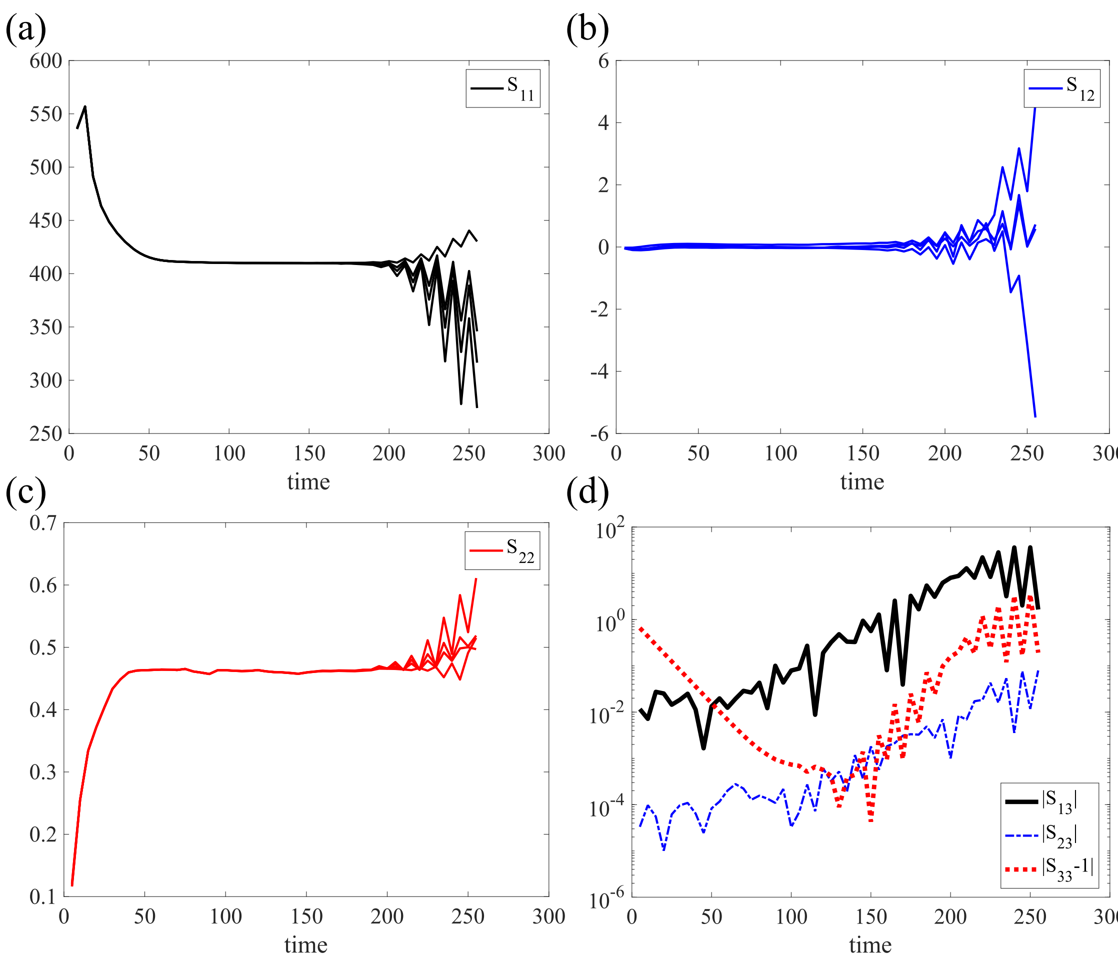

FIG. 10. Data from Oldroyd-B simulation described in Sec. III B 2 for Wi = 12. Temporal behavior of (a) S_{11}, (b) S_{12}, and (c) S_{22} components of the conformation tensor at $(x, y) = (\pi, \pi)$ plotted at 4 different z values between 0.88 and 3.14. (c) Temporal behavior of $|S_{13}|$, $|S_{23}|$, $|S_{33} - 1|$ components of the conformation tensor at $(x, y) = (\pi, \pi)$ for $z = 0.88$; note the log scale on the y-axis.

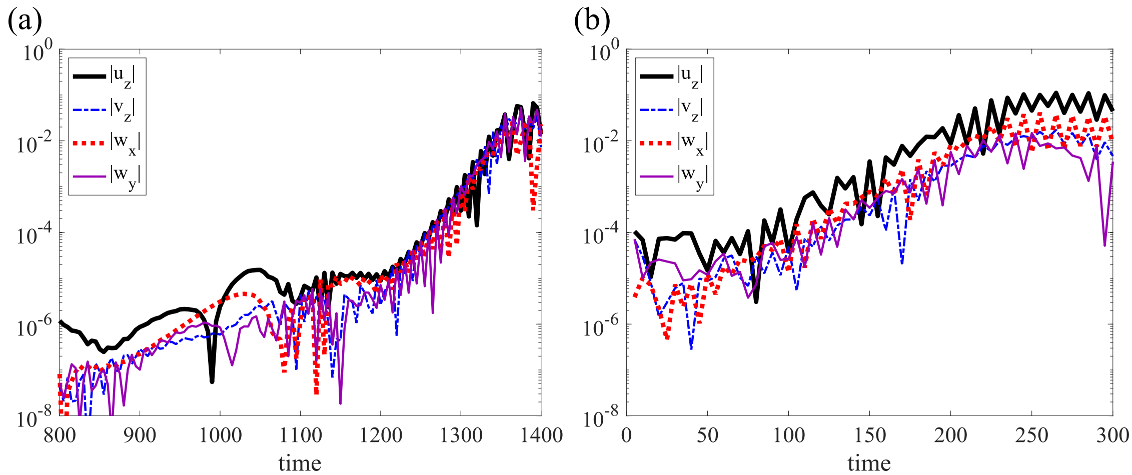

FIG. 11. Data from Oldroyd-B simulation described in Secs. III B 1 and III B 2 for (a) Wi = 8 and (b) Wi = 12. Temporal behavior of $\partial_z u$, $\partial_z v$, $\partial_x w$, $\partial_y w$ at $(x, y) = (\pi, \pi)$ for $z = 0.88$; note the log scale on the y-axis. These are components of the velocity gradient that are zero when there is no z-dependence in the flow.

and similarly for the velocity]. Then, we define the 3D conformation tensor as

$$\mathbf{S}^0 = \begin{bmatrix} \overline{S}^0_{11} & \overline{S}^0_{12} & 0 \\ \overline{S}^0_{12} & \overline{S}^0_{22} & 0 \\ 0 & 0 & 1 \end{bmatrix} \tag{7}$$

with the corresponding velocity

$$\mathbf{u}^0 = \begin{bmatrix} \overline{u}^0 \\ \overline{v}^0 \\ 0 \end{bmatrix}. \tag{8}$$

It is easy to see that $(\mathbf{u}^0, \mathbf{S}^0)$ will solve Eqs. (1)–(3) in 3D, given the 2D solution. Now, we consider perturbations around this background (numerical) solution, i.e., let

$$\mathbf{S} = \mathbf{S}^0 + \widetilde{\mathbf{S}}, \quad \text{and} \quad \mathbf{u} = \mathbf{u}^0 + \widetilde{\mathbf{u}}, \tag{9}$$

then the perturbation $(\widetilde{\mathbf{u}}, \widetilde{\mathbf{S}})$ satisfies

$$\Delta\widetilde{\mathbf{u}} - \nabla\tilde{p} + \beta\nabla\cdot\widetilde{\mathbf{S}} = 0, \tag{10}$$

$$\nabla\cdot\widetilde{\mathbf{u}} = 0, \tag{11}$$

$$\partial_t\widetilde{\mathbf{S}} + \mathrm{Wi}^{-1}\widetilde{\mathbf{S}} - \nu\Delta\widetilde{\mathbf{S}} = -\mathcal{N}(\mathbf{u}^0, \widetilde{\mathbf{S}}) - \mathcal{N}(\widetilde{\mathbf{u}}, \mathbf{S}^0) - \mathcal{N}(\widetilde{\mathbf{u}}, \widetilde{\mathbf{S}}), \tag{12}$$

where $\mathcal{N}(\mathbf{u}, \mathbf{S}) = \mathbf{u}\cdot\nabla\mathbf{S} - \left(\nabla\mathbf{u}\mathbf{S} + \mathbf{S}\nabla\mathbf{u}^T\right)$ are all the quadratic terms, and the nonlinear terms are given by $\mathcal{N}(\widetilde{\mathbf{u}}, \widetilde{\mathbf{S}})$. We do not have a closed form solution for $(\mathbf{u}^0, \mathbf{S}^0)$ necessitating a numerical study of the system. We numerically solve the linear system [i.e., Eqs. (10)–(12), but dropping the terms $\mathcal{N}(\tilde{u}, \tilde{S})$] from different initial conditions, and for different Wi, to see if small perturbations grow or decay. Here, we demonstrate, by an example where we perturb a single z-mode, that there is a linear instability in this system beyond a critical Wi. We show that with an initial perturbation only to a single mode in z of the 13-component of $\widetilde{\mathbf{S}}$, we have growth of the perturbation for Wi = 12 and decay of the perturbation for Wi = 8. This is not meant to be exhaustive but rather to indicate that there is a linear instability in this system and also to describe the behavior of the instability. A full analysis of the numerical eigenvalues–eigenfunctions is beyond the scope of this work.

We start with an initial perturbation of the form $\tilde{S}_{13}(x, y, z, 0) = \varepsilon \sin z$, with $\varepsilon = 0.001$. Solving the Stokes equation with this initial perturbation of the conformation tensor gives an initial perturbation to the velocity of the form $\tilde{u}(x, y, z, 0) = -\varepsilon\beta\cos z$, with $\tilde{v}, \tilde{w} \equiv 0$. When we examine the solutions with these initial data, we find that due to the structure of the equations, a "partition" of the z-axis is created, where initially some of the stress components grow where $\sin z \approx 1$ and some terms grow where $\cos z \approx 1$. This particular initial condition seems to accentuate this phenomenon. We next examine the structure of the equations that create/accentuate this partition.

The terms that grow where $\sin z \approx 1$ are $\tilde{S}_{13}$ and $\tilde{S}_{23}$, along with $\tilde{w}$ and $\partial_z\tilde{u}, \partial_z\tilde{v}, \partial_x\tilde{w}, \partial_y\tilde{w}$. We show contours of the (x, y) spatial dependence of these terms in Figs. 12 and 13. For Wi = 12, the perturbation grows and contours of $\tilde{S}_{13}(x, y, z^*, t_e)$ and $\tilde{S}_{23}(x, y, z^*, t_e)$ are shown in Figs. 12(a) and 12(b), where we choose $t_e = 24.5$ as a sample early time point and $z^* = \pi/2$. We note that the x, y structure of the $\tilde{S}_{13}$ term [Fig. 12(a)] is largest at the extensional point at (π, π) and extended along the y-axis, similar to the $\overline{S}^0_{11}$ component of the background solution. However, the x, y structure of the $\tilde{S}_{23}$ term, in Fig. 12(b), shows concentration along the axis of compression. As we see in Fig. 12(c), the instability has begun to grow, but it is early in the evolution of the instability. All other components of the conformation tensor are zero at z^* to machine precision at this time.

We also show components of the perturbation to the velocity gradients at this early time in Fig. 13. These four components, $\partial_z\tilde{u}, \partial_z\tilde{v}, \partial_x\tilde{w}, \partial_y\tilde{w}$ as well as $\tilde{w}$ (not shown) are the only non-zero components of the velocity gradient at z^*, t_e. We write the evolution of $\tilde{S}_{13}$ and $\tilde{S}_{23}$ out explicitly below as there is some simplification

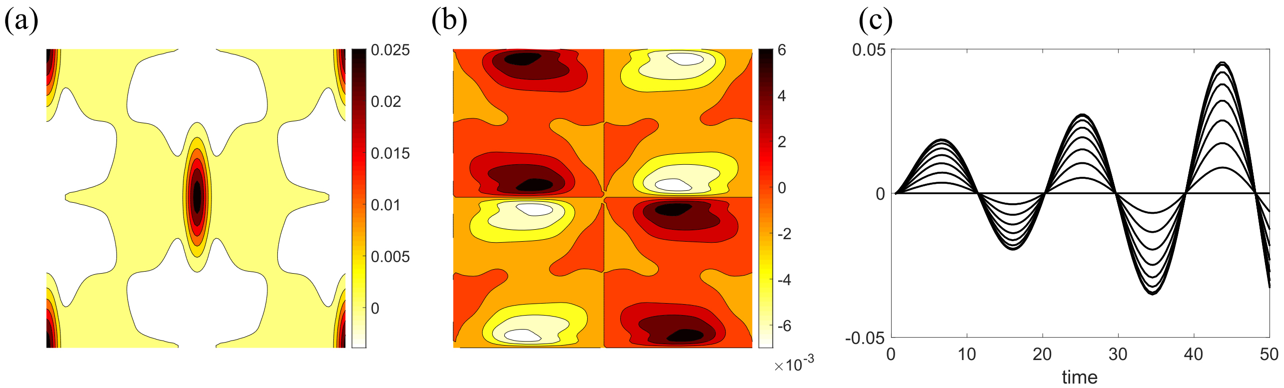

FIG. 12. Solutions from linear evolution of the Oldroyd-B system with Wi = 12. (a) Contours of $\tilde{S}_{13}(x, y, \pi/2, t_e)$ for t_e = 24.5, (b) contours of $\tilde{S}_{23}(x, y, \pi/2, t_e)$ for t_e = 24.5, and (c) $\tilde{S}_{13}(\pi, \pi, z, t)$, for several locations $0 < z < \pi$ and Wi = 12.

due to the structure of the background solution. In other words, we expand Eq. (12) as

$$\partial_t \tilde{S}_{13} + \frac{1}{\mathrm{Wi}}\tilde{S}_{13} - \eta\Delta\tilde{S}_{13} = -(\overline{u}^0\partial_x + \overline{v}^0\partial_y)\tilde{S}_{13} + \partial_x\tilde{w}\overline{S}^0_{11} + \partial_y\tilde{w}\overline{S}^0_{12} + \partial_z\tilde{u} + \partial_x\overline{u}^0\tilde{S}_{13} + \partial_y\overline{u}^0\tilde{S}_{23}, \tag{13}$$

$$\partial_t \tilde{S}_{23} + \frac{1}{\mathrm{Wi}}\tilde{S}_{23} - \eta\Delta\tilde{S}_{23} = -(\overline{u}^0\partial_x + \overline{v}^0\partial_y)\tilde{S}_{23} + \partial_x\tilde{w}\overline{S}^0_{12} + \partial_y\tilde{w}\overline{S}^0_{22} + \partial_z\tilde{v} + \partial_x\overline{v}^0\tilde{S}_{13} + \partial_y\overline{v}^0\tilde{S}_{23}, \tag{14}$$

Examining Eqs. (13) and (14), we note that it is exactly the above listed components of the velocity that are involved in the evolution

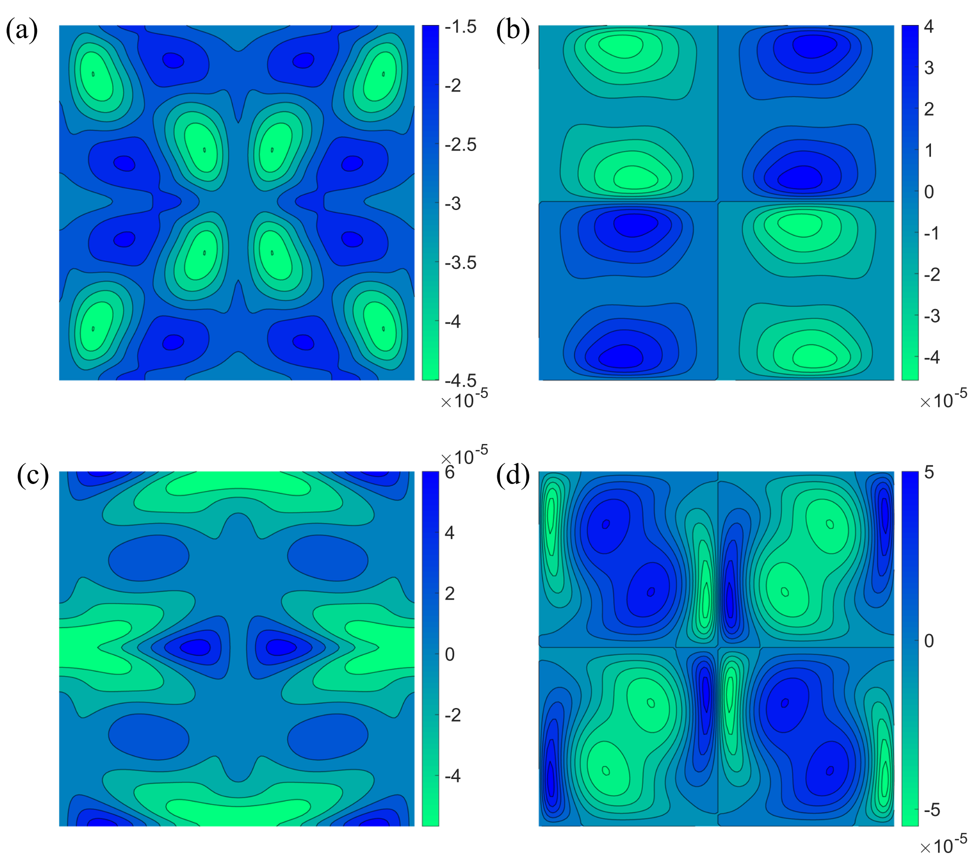

FIG. 13. Components of the velocity gradient at t_e = 24.5, Wi = 12. (a) $\partial_z\tilde{u}(x, y, \pi/2, t_e)$, (b) $\partial_z\tilde{v}(x, y, \pi/2, t_e)$, (c) $\partial_x\tilde{w}(x, y, \pi/2, t_e)$, and (d) $\partial_y\tilde{w}(x, y, \pi/2, t_e)$.

of $\tilde{S}_{13}, \tilde{S}_{23}$ at z^*. This implies a linear evolution of the components that has the form $e^{\alpha t} f(x, y) \sin z$ for short times. The real part of α is positive for Wi = 12 and the imaginary part is nonzero. However, the Stokes equation couples all of the stress components in a non-local manner and deriving exactly how α depends on the background solution is beyond the scope of this work. It is clear from the x, y spatial dependence of the components shown in Figs. 12 and 13 that the spatial structure of these terms is non-trivial and also relevant in the dynamics. In particular in Eq. (13), we see that the background $\overline{S}^0_{11}$ solution is driving the growth of $\tilde{S}_{13}$ via the term $\partial_x \tilde{w} \overline{S}^0_{11}$.

The spatial structure of these stress components is very similar (not shown) for Wi = 8 at early times, but the initial perturbation shows decaying oscillations, indicating that Wi = 8 is linearly stable with respect to this initial condition. This is shown in Fig. 14, where we display the evolution of the components above $(\pi, \pi, \pi/2)$, indicating that this perturbation decays for Wi = 8 [Figs. 14(a) and 14(b)] and grows for Wi = 12 [Figs. 14(c) and 14(d)].

We have simulated a range of Wi and have found that when Wi ≈ 9.7, the flow becomes linearly unstable to this perturbation, but we do not have a precise explanation for this value. Examining Eq. (13), we can see a cartoon of a possible instability criteria where the decay terms $-\frac{1}{\mathrm{Wi}}\tilde{S}_{13} + \eta\Delta\tilde{S}_{13}$ must be overcome by the other terms (for example) $\partial_x \tilde{w} \overline{S}^0_{11} + \partial_z \tilde{u} + \partial_x \overline{u}^0 \tilde{S}_{13}$, but again the coupling via Stokes equation and how $\tilde{w}, \tilde{u}$ depend on $\tilde{S}$ must be understood more fully before this argument can be made precise and predictive of the instability.

The evolution of the terms $\tilde{S}_{11}, \tilde{S}_{12}, \tilde{S}_{22}$ in the conformation tensor is given in Eqs. (15)–(17).

$$\begin{aligned}\partial_t \tilde{S}_{11} + \frac{1}{\mathrm{Wi}}\tilde{S}_{11} - \eta\Delta\tilde{S}_{11} = &-(\tilde{u}\partial_x + \tilde{v}\partial_y)\overline{S}^0_{11} - (\overline{u}^0\partial_x + \overline{v}^0\partial_y)\tilde{S}_{11} \\ &+ 2(\partial_x \tilde{u}\overline{S}^0_{11} + \partial_y \tilde{u}\overline{S}^0_{12}) \\ &+ 2(\partial_x \overline{u}^0 \tilde{S}_{11} + \partial_y \overline{u}^0 \tilde{S}_{12}),\end{aligned} \tag{15}$$

$$\begin{aligned}\partial_t \tilde{S}_{12} + \frac{1}{\mathrm{Wi}}\tilde{S}_{12} - \eta\Delta\tilde{S}_{12} = &-(\tilde{u}\partial_x + \tilde{v}\partial_y)\overline{S}^0_{12} - (\overline{u}^0\partial_x + \overline{v}^0\partial_y)\tilde{S}_{12} \\ &+ (\partial_x \tilde{u} + \partial_y \tilde{v})\overline{S}^0_{12} + \partial_x \tilde{v}\overline{S}^0_{11} \\ &+ \partial_y \tilde{u}\overline{S}^0_{22} + \partial_x \overline{v}^0 \tilde{S}_{11} + \partial_y \overline{u}^0 \tilde{S}_{22},\end{aligned} \tag{16}$$

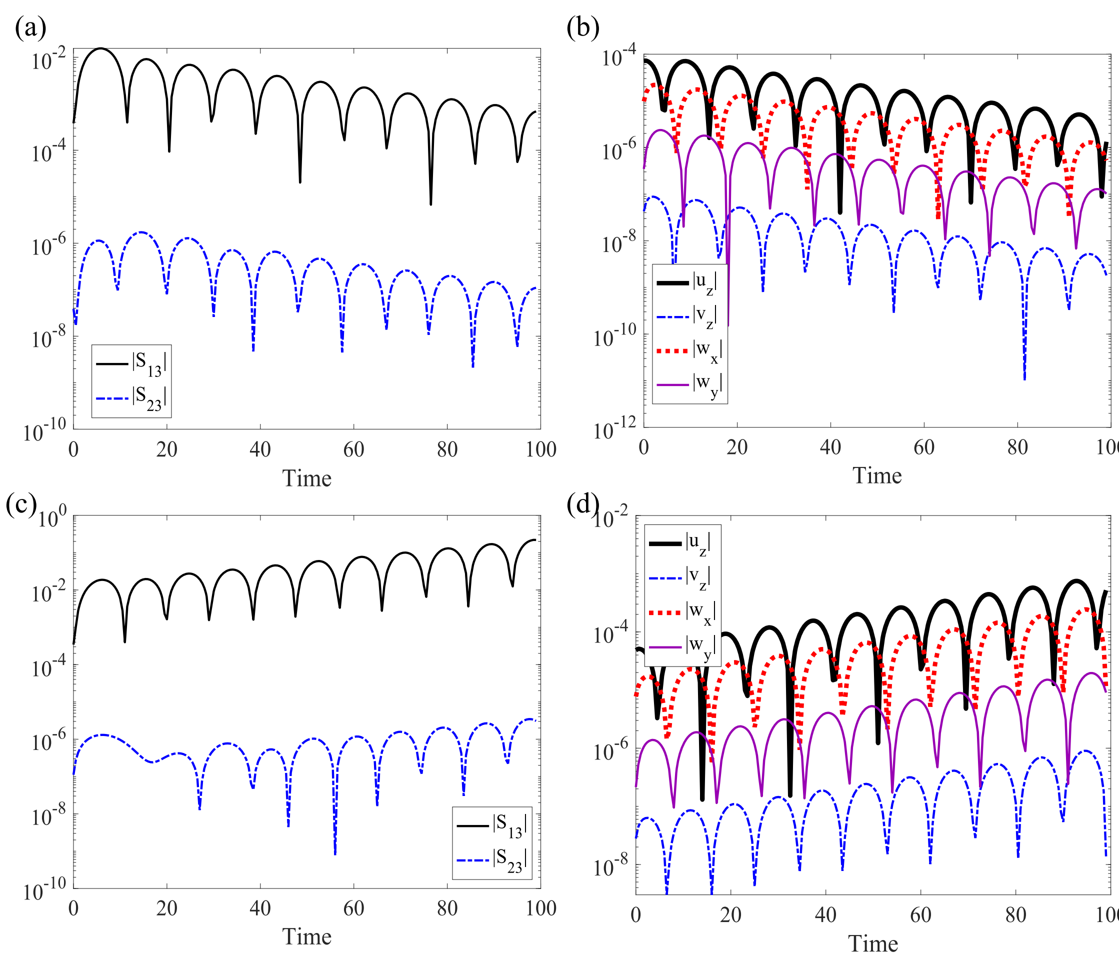

FIG. 14. (a) and (b) Wi = 8, (c) and (d) Wi = 12. Temporal evolution of linear perturbation for $|\tilde{S}_{13}|, |\tilde{S}_{23}, |\partial_z \tilde{u}|, |\partial_z \tilde{v}|, |\partial_x \tilde{w}|, |\partial_y \tilde{w}|$ at $(\pi, \pi, \pi/2)$.

$$\partial_t \tilde{S}_{22} + \frac{1}{\mathrm{Wi}}\tilde{S}_{22} - \eta\Delta\tilde{S}_{22} = -(\tilde{u}\partial_x + \tilde{v}\partial_y)\overline{S}^0_{22} - (\overline{u}^0\partial_x + \overline{v}^0\partial_y)\tilde{S}_{22} + 2(\partial_x\tilde{v}\overline{S}^0_{12} + \partial_y\tilde{v}\overline{S}^0_{22}) + 2(\partial_x\overline{v}^0\tilde{S}_{12} + \partial_y\overline{v}^0\tilde{S}_{22}). \tag{17}$$

All these terms have z-dependence like $\cos z$ on short times, and this is due to the fact that at $t = 0$, $\tilde{u}(x, y, z, 0) = -\varepsilon\beta\cos z$, which introduces the z-dependence into all of these terms. However, the growth of the instability does not appear to be tied to these terms because these terms are effectively acting only in the x, y plane.

Finally, the $\tilde{S}_{33}$ component evolves according to the following equation:

$$\partial_t \tilde{S}_{33} + \frac{1}{\mathrm{Wi}}\tilde{S}_{33} - \eta\Delta\tilde{S}_{33} = -(\overline{u}^0\partial_x + \overline{v}^0\partial_y)\tilde{S}_{33} + 2\partial_z\tilde{w}. \tag{18}$$

As $\tilde{S}_{13}$ becomes spatially dependent, the z-dependence enters $\tilde{w}$ via the Stokes equation, and hence (matching derivatives) $\tilde{w}$ will depend on z as $\tilde{S}_{13}$ via $\sin z$, and hence $\partial_z\tilde{w} \sim \cos z$. The growth of $\tilde{S}_{33}$ is essential to the linear instability, and this is where a criterion for instability is most likely to be found. If we can analytically understand the relationship between $\partial_z\tilde{w}$ and $\tilde{S}_{33}$, then a criterion related to Wi seems likely to follow this.

The perturbative terms in Eqs. (15)–(18) are all largest (in absolute value) at $z = 0$, consistent with the z-structure $\sim\cos z$, and this is precisely where the previous terms $(\tilde{S}_{13}, \tilde{S}_{23}, \tilde{w}, \partial_z\tilde{u}, \partial_z\tilde{v}, \partial_x\tilde{w}, \partial_y\tilde{w})$ are zero (to machine precision). In Fig. 15 we show the evolution of these components at $(\pi, \pi, 0)$ for Wi = 8 and Wi = 12. Again, we find that the perturbation decays for Wi = 8 [(a) and (b)] and grows for Wi = 12 [(c) and (d)].

We find that the linear equations can be run on a coarse mesh, i.e., $N = 32$ grid points in each dimension, with results consistent with high resolution simulations, i.e., predicting that the flow is linearly stable for Wi = 8 and unstable for Wi = 12. The stress diffusion is also not necessary in these calculations and the linear simulations with zero stress diffusion still show stability for Wi = 8 and instability for Wi = 12.

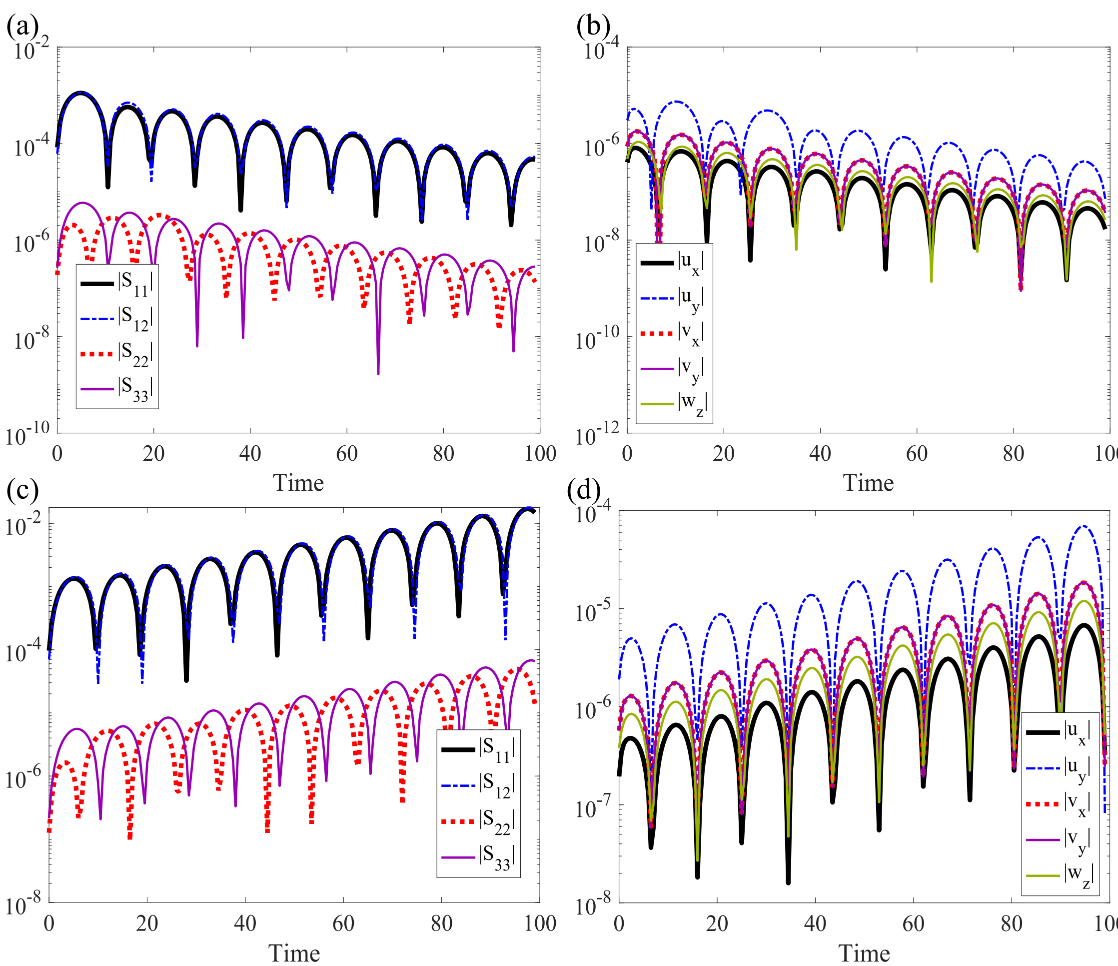

FIG. 15. (a) and (b) Wi = 8, (c) and (d) Wi = 12. Temporal evolution of linear perturbation for $|\tilde{S}_{11}|, |\tilde{S}_{12}|, |\tilde{S}_{22}|, |\tilde{S}_{33}|, |\partial_x\tilde{u}|, |\partial_y\tilde{u}|, |\partial_x\tilde{v}|, |\partial_y\tilde{v}|, |\partial_z\tilde{w}|$ at $(\pi, \pi, 0)$.

VI. CONCLUSION

We have analyzed the dynamics for a viscoelastic fluid at zero Reynolds number in a 3D periodic geometry with a 3D 4-roll mill background force. For small Wi, the flow is steady or has a temporal behavior confined to the x, y directions. However, for sufficiently large Wi, three-dimensional instabilities (instabilities in the z direction) occur. This three-dimensional instability is maintained in time and robust in the sense that it was found with both Oldroyd-B and FENE-P models, using different initial conditions and using different simulation techniques (i.e., both usual formulation and the square root formulation).

For the solutions analyzed using the Oldroyd-B model with $8 \leq \mathrm{Wi} < 10$, the flow develops x, y temporal behavior first, with a dominant vortex rotating around the four quarters, and then the z instability emerges creating three-dimensional behavior, where both instabilities are acting simultaneously. However, for $\mathrm{Wi} > 10$, the z-instability comes first, with an x, y instability occurring later. For solutions using the FENE-P model, we see the z instability but a simpler periodic state evolves with no significant x, y instability, nor any single dominant vortex.

Finally, we analyzed a particular initial condition that leads to a linear instability in the z direction beyond a critical Wi. This linear instability arises when the background flow is constant in z, but highly concentrated along the axis of extension, indicating that it is instability for the extensional flow geometry. This is a complicated system to analyze for the 4-roll mill solution at zero Reynolds number because the Stokes equation instantly couples all components of the velocity gradient with the stress tensor. The demonstration of a linear instability from the extensional background flow is a first step in understanding this three-dimensional instability.

ACKNOWLEDGMENTS

This work was partially supported by NSF (Grant No. DMS-1664679).

APPENDIX: IMPLEMENTATION DETAILS USING GPU

Our simulations require several Fast Fourier Transforms (FFT) and inverses (IFFT) in each iteration. This is because our model evolves entirely in Fourier space, which requires that all nonlinear terms in the upper-convected derivative are handled by performing the multiplications in real space and, subsequently, inverting the product to advect in Fourier space, with appropriate filtering. In previous, non-parallel implementations, it was found that computing FFTs (from now on, used as a generalization of FFT and IFFT) in long datasets was the largest bottleneck with regard to the runtime. For this reason, it was decided to parallelize the code, so it could run on a Graphics Processing Unit (GPU). Although a Central Processing Unit (CPU) can perform each specific addition/multiplication several times faster than a GPU, a GPU can perform between hundreds and thousands of these operations at the same time. In particular, GPUs are specialized for divide-and-conquer algorithms, such as FFT, allowing speeds ups beyond those available from CPUs or even multi-core CPUs.

GPU aided computation is already a well known and well-documented tool, and many programming languages/platforms geared toward computational endeavors have built-in Application Programming Interfaces (APIs), which directly interact with GPUs. In particular, the recent versions of MATLAB have built-in support for GPU computing, in a form resembling the typical MATLAB language/design philosophy. MATLAB's GPU computing API automatically calibrates several of MATLAB's native functions to most optimally run on the GPU (e.g., FFT and IFFT). Furthermore, MATLAB's language natively has N-D matrix data-structures with their corresponding operations, and its GPU computing API smoothly accommodates these structures with minimal alterations from the user. For these reasons, we developed a GPU implementation of our spectral code using MATLAB.

TABLE II. 2D simulation speed ups on a run for $0 \leq t \leq 5$.

Resolution	CPU (s)	GPU (s)	Speed-up
128 × 128	11.2275	3.551 22	×3.166
256 × 256	98.8118	10.015 7	×9.866
512 × 512	1904.8	42.148 5	×45.193

We provide a few more details for the interested reader. To speed up the calculations, repetitively calculated or defined variables were initialized at the start and stored on the GPU preemptively. Any quantities to be computed on the GPU were computed from quantities/variables already stored on the GPU. Even simple matrices, such as the identity, were stored on the GPU at the start of the program. This was done for two reasons. First, CPU to GPU data transfer rates are slow relative to the normal internal CPU data transfer rates. Second, GPU memory allocation is considerably slower than the CPU memory allocation. Furthermore, stressing awareness of the previous issue, GPUs have a small amount of onboard memory compared to a CPU. For example, the specific GPUs used in the implementation for this paper has only about 8 GB of available memory, meaning that only that much data can be initialized on the GPU. Last, GPUs have a smaller memory bandwidth. In other words, performing operations on larger datasets is slower than the trends established on smaller datasets would suggest. In other words, there are diminishing returns in performance beyond a certain threshold amount of data. The significance of this issue varies significantly between different models of GPUs.

Overall, the GPU implementation of our simulations significantly outperformed the CPU implementation, as illustrated in Table II. We performed our speed up tests on the 2D problem so that we could use fine grids. This was also to test the accuracy of the code by comparing with the CPU version. The finest grid $512^2 = 64^3$ showed a 45× speed up for the simulation. These types of speed ups allowed us to run our long-time simulations on grids 128^3.

REFERENCES

[1] B. Qin, P. Salipante, S. Hudson, and P. Arratia, "Upstream vortex and elastic wave in the viscoelastic flow around a confined cylinder," J. Fluid Mech. **864**, R2 (2019).
[2] R. J. Poole, "Three-dimensional viscoelastic instabilities in microchannel," J. Fluid Mech. **870**, 1–4 (2019).
[3] S. C. Omowunmi and X. F. Yuan, "Modelling the three-dimensional flow of a semi-dilute polymer solution in microfluidics-on the effect of aspect ratio," Rheol. Acta **49**, 585–595 (2010).

[4]F.-C. Li, H.-N. Zhang, Y. Cao, T. Kunugi, H. Kinoshita, and M. Oshima, "A purely elastic instability and mixing enhancement in a 3D curvilinear channel flow," Chin. Phys. Lett. **29**, 094704 (2012).
[5]D. Tang, F. H. Marchsini, L. Cardon, and D. R. D'hooge, "Three-dimensional flow simulations for polymer extrudate swell out of slit dies from low to high aspect ratios," Phys. Fluids **31**, 093103 (2019).
[6]S. J. Haward, K. Toda-Peters, and A. Q. Shen, "Steady viscoelastic flow around high-aspect-ratio, low-blockage-ratio microfluidic cylinders," J. Non-Newtonian Fluid Mech. **254**, 23–35 (2018).
[7]L. Pan, A. Morozov, C. Wagner, and P. E. Arratia, "Nonlinear elastic instability in channel flows at low Reynolds numbers," Phys. Rev. Lett. **110**(17), 174502 (2013).
[8]S. De, J. A. M. Kuipers, E. A. J. F. Peters, and J. T. Padding, "Viscoelastic flow simulations in model porous media," Phys. Rev. Fluids **2**(5), 053303 (2017).
[9]P. E. Arratia, C. C. Thomas, J. Diorio, and J. P. Gollub, "Elastic instabilities of polymer solutions in cross-channel flow," Phys. Rev. Lett. **96**(14), 144502 (2006).
[10]R. J. Poole, M. A. Alves, and P. J. Oliveira, "Purely elastic flow asymmetries," Phys. Rev. Lett. **99**(16), 164503 (2007).
[11]L. Xi and M. D. Graham, "A mechanism for oscillatory instability in viscoelastic cross-slot flow," J. Fluid Mech. **622**, 145–165 (2009).
[12]A. M. Alfonso, M. A. Alves, and F. T. Pinho, "Purely elastic instabilities in three-dimensional cross-slot geometries," J. Non-Newtonian Fluid Mech. **165**, 743–751 (2010).
[13]P. C. Sousa, F. T. Pinho, and M. A. Alves, "Purely-elastic flow instabilities and elastic turbulence in microfluidic cross-slot devices," Soft Matter **14**(8), 1344–1354 (2018).
[14]B. Thomases and M. Shelley, "Emergence of singular structures in Oldroyd-B fluids," Phys. Fluids **19**(10), 103103 (2007).
[15]B. Thomases and M. Shelley, "Transition to mixing and oscillations in a Stokesian viscoelastic flow," Phys. Rev. Lett. **103**(9), 094501 (2009).
[16]B. Thomases, M. Shelley, and J.-L. Thiffeault, "A Stokesian viscoelastic flow: Transition to oscillations and mixing," Physica D **240**(20), 1602–1614 (2011).
[17]B. Thomases, "An analysis of the effect of stress diffusion on the dynamics of creeping viscoelastic flow," J. Non-Newtonian Fluid Mech. **166**(21), 1221–1228 (2011).
[18]J. A. Biello and B. Thomases, "Equilibrium circulation and stress distribution in viscoelastic creeping flow," J. Non-Newtonian Fluid Mech. **229**, 101–111 (2016).
[19]R. B. Bird, P. J. Dotson, and N. L. Johnson, "Polymer solution rheology based on a finitely extensible bead–spring chain model," J. Non-Newtonian Fluid Mech. **7**(2-3), 213–235 (1980).
[20]N. Balci, B. Thomases, M. Renardy, and C. R. Doering, "Symmetric factorization of the conformation tensor in viscoelastic fluid models," J. Non-Newtonian Fluid Mech. **166**(11), 546–553 (2011).
[21]P. Gutierrez-Castillo and B. Thomases, "Proper orthogonal decomposition (POD) of the flow dynamics for a viscoelastic fluid in a four-roll mill geometry at the Stokes limit," J. Non-Newtonian Fluid Mech. **264**, 48–61 (2019).